



Revealing the role of necroptosis microenvironment: FCGBP + tumor-associated macrophages drive primary liver cancer differentiation towards cHCC-CCA or iCCA

Chun Wang¹ · Cuimin Chen¹ · Wenting Hu¹ · Lili Tao¹ · Jiakang Chen¹

Accepted: 17 October 2023 / Published online: 28 November 2023

© The Author(s), under exclusive licence to Springer Science+Business Media, LLC, part of Springer Nature 2023

Abstract

Previous research has demonstrated that the conversion of hepatocellular carcinoma (HCC) to intrahepatic cholangiocarcinoma (iCCA) can be stimulated by manipulating the tumor microenvironment linked with necroptosis. However, the specific cells regulating the necroptosis microenvironment have not yet been identified. Additionally, further inquiry into the mechanism of how the tumor microenvironment regulates necroptosis and its impact on primary liver cancer (PLC) progression may be beneficial for precision therapy. We recruited a single-cell RNA sequencing dataset (scRNA-seq) with 34 samples from 4 HCC patients and 3 iCCA patients, and a Spatial Transcriptomic (ST) dataset including one each of HCC, iCCA, and combined hepatocellular-cholangiocarcinoma (cHCC-CCA). Quality control, dimensionality reduction and clustering were based on Seurat software (v4.2.2) process and batch effects were removed by harmony (v0.1.1) software. The pseudotime analysis (also known as cell trajectory) in the single cell dataset was performed by monocle2 software (v2.24.0). Calculation of necroptosis fraction was performed by AUCell (v1.16.0) software. Switch gene analysis was performed by geneSwitches(v0.1.0) software. Dimensionality reduction, clustering, and spatial image in ST dataset were performed by Seurat (v4.0.2). Tumor cell identification, tumor subtype characterization, and cell type deconvolution in spot were performed by SpaCET (v1.0.0) software. Immunofluorescence and immunohistochemistry experiments were used to prove our conclusions. Analysis of intercellular communication was performed using CellChat software (v1.4.0). ScRNA-seq analysis of HCC and iCCA revealed that necroptosis predominantly occurred in the myeloid cell subset, particularly in FCGBP + SPP1 + tumor-associated macrophages (TAMs), which had the highest likelihood of undergoing necroptosis. The existence of macrophages undergoing necroptosis cell death was further confirmed by immunofluorescence. Regions of HCC with poor differentiation, cHCC-CCA with more cholangiocarcinoma features, and the tumor region of iCCA shared spatial colocalization with FCGBP + macrophages, as confirmed by spatial transcriptomics, immunohistochemistry and immunofluorescence. Pseudotime analysis showed that premalignant cells could progress into two directions, one towards HCC and the other towards iCCA and cHCC-CCA. Immunofluorescence and immunohistochemistry experiments demonstrated that the number of macrophages undergoing necroptosis in cHCC-CCA was higher than in iCCA and HCC, the number of macrophages undergoing necroptosis in cHCC-CCA with cholangiocarcinoma features was more than in cHCC-CCA with hepatocellular carcinoma features. Further investigation showed that myeloid cells with the highest necroptosis score were derived from the HCC_4 case, which had a severe inflammatory background on pathological histology and was likely to progress towards iCCA and cHCC-CCA. Switchgene analysis indicated that S100A6 may play a significant role in the progression of premalignant cells towards iCCA and cHCC-CCA. Immunohistochemistry confirmed the expression of S100A6 in PLC, the more severe inflammatory background of the tumor area, the more cholangiocellular carcinoma features of the tumor area, S100A6 expression was higher. The emergence of necroptosis microenvironment was found to be significantly associated with FCGBP + SPP1 + TAMs in PLC. In the presence of necroptosis microenvironment, premalignant cells appeared to transform into iCCA or cHCC-CCA. In contrast, without a necroptosis microenvironment, premalignant cells tended to develop into HCC, exhibiting amplified stemness-related genes (SRGs) and heightened malignancy.

Chun Wang and Jiakang Chen contributed equally to this work.

Extended author information available on the last page of the article

Keywords Necroptosis · PLC · ScRNA-seq · ST · FCGBP · TAMs · Pseudotime · GeneSwitches · Immunofluorescence

Abbreviations

scRNA-seq	Single-cell RNA sequencing
ST	Spatial transcriptome
PLC	Primary liver cancer
HCC	Hepatocellular carcinoma
iCCA/iCC	Intrahepatic cholangiocarcinoma
CNV	Copy number variation
TCGA	The cancer genome atlas
TAM	Tumor-associated macrophage
CAF	Cancer associated fibroblasts
TIB	Tumor immune barrier
LAM	Lipid associated macrophages
TAME	Tumor-adipose microenvironment
SRG	Stemness-related gene
GEO	Gene expression omnibus
HE	Hematoxylin–eosin staining

Introduction

PLC remains by far one of the most prevalent and lethal cancers, consisting mainly of HCC, iCCA and cHCC-CCA, with HCC and iCCA accounting for approximately 80% and 15%, respectively [1, 2]. The cHCC-CCA consists of three subtypes, separated, combined and mixed subtypes. cHCC-CCA has been shown to be of monoclonal origin for both combined and mixed cHCC-CCA [3]. However, to date, the cellular origin and genetic alterations of these three PLC tumors are still not well understood, leaving us without specific markers for pathological diagnosis when tumor is poorly differentiated, and cannot further support clinical precision treatment. YAP activation leads to the transition of mature hepatocytes to hepatic progenitor cells, while intrinsic differences in Sox9 expression determines the tumor type [4]. Other studies have also explored the molecular mechanisms of iCCA and CHC development, the activation of genes like NOTCH, AKT and c-Myc possibly contributes to the formation of partial iCCA [5–7]; Kras and TP53 may be key regulators of iCCA which originated from hepatocytes [8]; TGF- β and Wnt/ β -catenin were identified as the two major signaling pathways involved in cHCC-CCA [9]; Blocking NF- κ B signaling modifies the morphological transformation of c-Myc-driven HCC to cHCC-CCA [10]; AKT and Ras pathway activation accelerated tumor progression toward cHCC-CCA [11, 12]. Previous studies have showed that HCC, iCCA, and cHCC-CCA may all originate from hepatocytes, but a systematic and detailed transformation process remains incomplete.

Transarterial chemoembolization (TACE) is a standard treatment for intermediate-stage HCC, but not all patient benefits from it [13]. In some cases, TACE treatment has been showed to increase the expression of hypoxia-inducible factors (HIF1- α and COX-2), which can promote cancer angiogenesis, inhibit cancer cell apoptosis, and enhance invasion and migration [14]. Alexei et al. demonstrated that in the absence of intracellular apoptotic signaling, it is capable of activating a common nonapoptotic death pathway, which they termed necroptosis [15].

Necroptosis, a form of cell death, may promote tumorigenesis and cancer metastasis through inflammatory responses, but its role varied in different tumor [16, 17]. The necrosome composed of RIPK1 and RIPK3 phosphorylates MLKL, pMLKL translocates to cell membranes, thereby resulting in cell perforation damage and inducing inflammatory responses, which is the classical pathway of necroptosis [18, 19]. Susana et al. reported that necroptotic cells could continue to produce cytokine even after they had lost cell membrane integrity and irreversibly committed to death. Cell death and production of inflammatory mediators were coordinated to optimize the immunogenicity of necroptotic cells [20]. Furthermore, Marco et al. found that necroptosis-associated hepatic cytokine microenvironment determined ICC outgrowth from oncogenically transformed hepatocytes, and hepatocytes containing identical oncogenic drivers gave rise to HCC if they were surrounded by apoptotic hepatocytes through mouse experiments [21]. We hypothesize that the necroptosis-associated hepatic microenvironment may be induced by cytokines produced by cells undergoing necroptosis.

To further investigate this hypothesis, we analyzed differences in gene expression at single-cell and spatial levels using ScRNA-seq and ST data from human PLC comprehensively for the first time. Our aim is to explore the subsets of cells that may undergo necroptosis, the potential evolutionary trajectory of PLC tumor cells, the association between necroptosis microenvironment and tumor progression, and the markers that can be used to identify different PLC subtypes.

Materials and methods

Data collection

The ScRNA-seq dataset (GSE189903) including HCC and iCCA was collected from the Gene Expression Omnibus

database (<https://www.ncbi.nlm.nih.gov/geo/>). The ST dataset including HCC, iCCA and cHCC-CCA (HRA000437) was collected from the Genome Sequence Archive (GSA).

(<https://ngdc.cncb.ac.cn/gsa-human/browse/HRA000437>).

ScRNA and ST data processing

Data analysis of single-cell transcriptomics was performed by using R(v4.2.2). Quality control, dimensionality reduction and clustering were based on Seurat software (v4.0.2) process and batch effects were removed by harmony (v0.1.1) software. Quality control conditions included: ① The number of genes detected in each cell was not less than 200; ② The number of genes detected in each cell was no more than 6000; ③ The proportion of mitochondrial genes detected in each cell was not more than 15%. Determination of the optimal number of dimensionality reduction and clustering subsets for epithelial cells and myeloid cells was performed by clustree (v0.5.0) software. The Spatial transcriptomics data were converted into Seurat objects by using Seurat software (v4.2.2) and normalised by using SCTransform algorithm. Different celltypes were identified by common cell-specific marker genes in combination with manual calibration. The genes characteristic of cell subsets were identified simultaneously by using COSG (v0.9.0) software and the 'FindAllMarkers' function of Seurat software, in combination with the celltype identification databases 'CellMarker' and 'SingleCellBase' to determined the type of cell subsets. Gene function enrichment analyses used the clusterProfiler(v4.9.3) software.

Identification of the degree of HCC differentiation

We identified the degree of differentiation of cancer in different HCC cases based on the definition in WHO Classification of Tumours of the Digestive Dystem [22]. In highly differentiated HCC, cancer cells are slightly atypia, arranged in small trabeculae, and pseudoglandular structures are common. Intermediate-differentiated HCC is commonly with moderate atypia, abundant eosinophilic cytoplasm, rounded nuclei, and obvious nucleoli, arranged in trabeculae by three or more layers of cells. Poorly differentiated HCC shows solid growth with higher atypia and no obvious blood sinus-like lacunes. Poorly differentiated component is often centrally located, while highly differentiated component is peripherally located.

Developmental trajectory inference

To characterize the potential lineage differentiation among diverse cells, we used monocle2 (v2.24.0) software to

perform a potential lineage differentiation study of epithelial and myeloid cells.

Necroptosis scores

The AUCell (v1.16.0) was used to calculate the enrichment fraction of the necroptosis gene set in different cell subsets. The necroptosis gene set was obtained from the KEGG entry: hsa04217.

Identification of cell types in ST spot

Due to the unique property of ST such that each spatial Spot contained multiple cell signals simultaneously, we used SpaCET (v1.0.0) software to identify the cell types contained in each spot of ST dataset. SpaCET estimated the proportion of malignant cells by predicting the copy number variation (CNV) in each spot initially, which relied on the dictionary of gene specific features including gene CNVs and gene expression patterns for different cancer types, which was constructed by The Cancer Genome Atlas (TCGA) Based on the correlation between genetic features, we identified malignant spots associated with specific tumor types, and the percentage of malignant cells in each spot. In addition, SpaCET used a linear regression model to hierarchically resolve the percentage of non-malignant cells in each Spot. Multiple ScRNA-seq datasets had been built and integrated in SpaCET to provide convenient access for users to obtain reference expression profiles of various cell types required for regression calculations.

Switch-genes analysis

GeneSwitches was an R software to calculate on/off time sequences of key gene expressed in pseudotime analysis. We used GeneSwitches(v0.1.0) software to analyze switch genes during changes of different pseudotime states in the trajectory of epithelial cells. GeneSwitches software firstly screened potential switch genes that had both on and off states of expression characteristics by binarizing the genes in trajectory, then performed logistic regression analysis and McFadden's Pseudo R2 pseudotime correlation analysis on these potential switch genes, eventually deduced switching time point of each switch gene by logistic regression analysis.

Immunofluorescence and immunohistochemistry

All samples were obtained from the Department of Pathology, Peking University Shenzhen Hospital, and all diagnoses were individually confirmed and jointly reviewed by three senior pathologists. We collected paraffin sections from 3 cases of HCC, 1 case of iCCA and 2 cases of cHCC-CCA,

and performed immunofluorescence staining for CD68 and pMLKL. The CD68 reagent used was Recombinant Anti-CD68 antibody [KP1] (ab955) from Abcam. The pMLKL reagent used was Recombinant Anti-MLKL (phospho S358) antibody [EPR9514] (ab187091) from Abcam. After continuous sectioning (thickness 3µm) of formalin-fixed paraffin-embedded (FFPE) blocks, deparaffinization was performed with xylene. Antigen retrieval was done using EDTA antigen retrieval solution (MXB MVS-0099). 2% EDTA antigen retrieval buffer was preheated in a microwave oven to 95 °C; sections were placed in preheated EDTA, heated to boiling, and taken out after 20 min. Sections were then cooled to room temperature; washed 3 times with PBS, 5 min each time; permeabilized with 0.25% Triton-PBS for 20 min; washed 3 times with PBS, 5 min each time; blocked with 3% BSA solution for 30 min; primary antibodies were diluted to recommended concentrations and sections were incubated at 4 °C for 24–48 h; after incubation, sections were washed 3 times with PBS, 5 min each time; sections were then incubated with secondary antibodies (CoraLite488-conjugated Goat Anti-Rabbit IgG(H+L) and CoraLite594-conjugated Goat Anti-Mouse IgG(H+L), Proteintech) diluted in PBS, at room temperature protected from light for 2 h; after incubation, sections were washed 3 times with PBS, 5 min each time; sections were mounted with antifade mounting medium with DAPI; images were observed and captured under fluorescence microscope at 40× magnification. We collected paraffin sections from 3 cases of HCC, 2 cases of iCCA and 4 cases of cHCC-CCA (including 2 cases of combined type and 2 cases of mixed type) and performed immunohistochemical staining for CD68, pMLKL, FCGBP, S100A6 and SPP1. The CD68 reagent used was Recombinant Anti-CD68 antibody [KP1] (ab955) from Abcam. The pMLKL reagent used was Recombinant Anti-MLKL (phospho S358) antibody [EPR9514] (ab187091) from Abcam. The FCGBP reagent used was Anti-FCGBP antibody produced in rabbit(HPA003517) from Sigma-Aldrich. The S100A6 reagent used was Anti-S100 alpha 6/PRA antibody [EPR13084-69] (ab 181,975) from Abcam. The SPP1 reagent used was Recombinant Anti-Osteopontin antibody [EPR21139-316] (ab214050) from Abcam. Immunohistochemistry was carried out using a Ventana BenchMark ULTRA automated immunostaining system, following the manufacturer's recommendation (Ventana Medical Systems, Tucson, AZ, USA). The primary antibody was diluted to 1:200.

Cell–cell interaction analysis

CellChat(v1.4.0) software was used to infer, analyze and visualize intercellular communication interactions between cell subsets in ScRNA-seq. 'Seurat' normalized expression matrices were used for ligand-receptor interaction analysis.

The list of known ligand-receptor pairs was obtained from CellChatDB, a literature-supported database of mouse and human ligand and receptor interactions. We first identified overexpressed ligands or receptors in cell types and inferred communication probabilities by calculating all ligand and receptor interactions associated with each signaling pathway.

Results

Exploring the necroptosis landscape in the single-cell atlas of PLC

We recruited a ScRNA-seq dataset including 4 HCC samples and 3 iCCA samples [23]. A total of approximately 112,200 cells were obtained after rigorous data cleaning, quality control and batch effect removal (Supplementary Material S1). All cells were dimensionality reduction and clustering by using Seurat software, a total of 32 cell subsets were identified (Fig. 1A, marker genes were identified by COSG, the results are detailed in Supplementary Material S2). Based on consensus cell specific marker genes, these 32 cell subsets were classified into 8 cell types, including cholangiocytes, endothelial cells, fibroblasts, hepatocytes, plasmacytoid dendritic cells and myeloid cells (Fig. 1B). The cell specific marker genes used were as follows, myeloid cells: CD4, CD14, CD68, CD163; T/NK cells: PTPRC, CD3D, CD8A, NKG7; B cells: CD79A, MS4A1; hepatocytes: ALB, MT-ATP8, ARG1, AFP; fibroblasts: COL1A1, ACTA2, ACTG2; endothelial cells: CD34, PECAM. CDH5; cholangiocytes: EPCAM, KRT7, KRT19; plasmacytoid dendritic cells: CLEC4C, CD4, CD68 (Fig. 1C). By mapping cell information from different samples to uniform manifold approximation and projection (UMAP), the result (Fig. 1D) showed that HCC and iCCA shared the majority of cell types, but a small portion of T/NK cells were unique in iCCA which deserved more attention in the future. Furthermore, we observed the expression of the core regulatory genes of necroptosis in all cell types, including RIPK1, RIPK3 and MLKL (Fig. 1E). MLKL was highest expressed in myeloid cells and endothelial cells as the main executor of necroptosis, while RIPK3, which motivates MLKL to be phosphorylated into pMLKL, was relatively highly expressed in myeloid cells. Considering that myeloid cells were much more abundant than endothelial cells in the single cell atlas, we deduced that myeloid cells were the major cell type that underwent necroptosis in PLC. Although MLKL acted as the main executor of necroptosis, necroptosis process was not only related to the function of MLKL, but also to biological changes such as mitochondrial damage, inflammatory response, and enhanced lysosomal membrane permeability (Supplementary Material S3). To further verify our findings, we obtained the gene collection consisting of

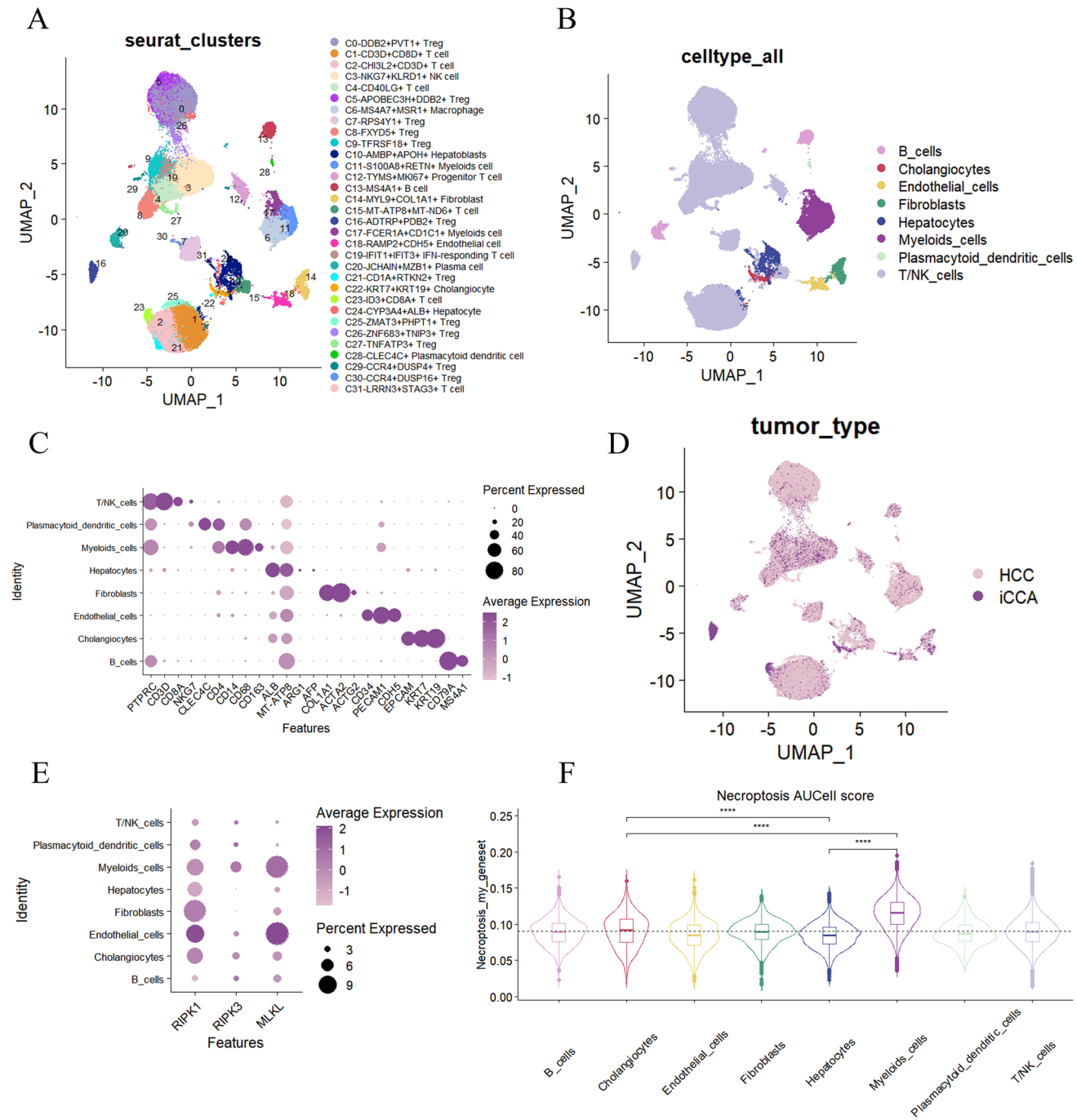


Fig 1 Necroptosis microlandscape in PLC single cell atlas. **A** A total of 32 subsets obtained by dimensionality reduction and clustering in single cell datasets of HCC and iCCA. **B** A preliminary annotation of the types of 32 cell subsets was made based on common marker genes. **C** Celltype annotation by marker genes, the darker the purple colour, the higher the gene expression, and the size of the dot represents the percentage of cells expressing the gene for that celltype. **D**

Sample origin information for each cell was mapped to UMAP. **E** The expression of RIPK1, RIPK3 and MLKL, which were mainly associated with necroptosis in all celltypes. **F** Violin plot showed the comprehensive score of 159 necroptosis-associated genes in all celltypes by using AUCell software (*, $P < 0.05$; **, $P < 0.01$; ***, $P < 0.001$; ****, $P < 0.0001$; ns, $P > 0.05$) (Color figure online)

159 necroptosis gene from KEGG official website as entry hsa04217 (Supplementary Material S4) and calculated the necroptosis score for all cell types with AUCell software

(Fig. 1F). Our results showed that myeloid cells got the highest necroptosis score, which was significantly higher than hepatocytes and cholangiocytes, tentatively demonstrating

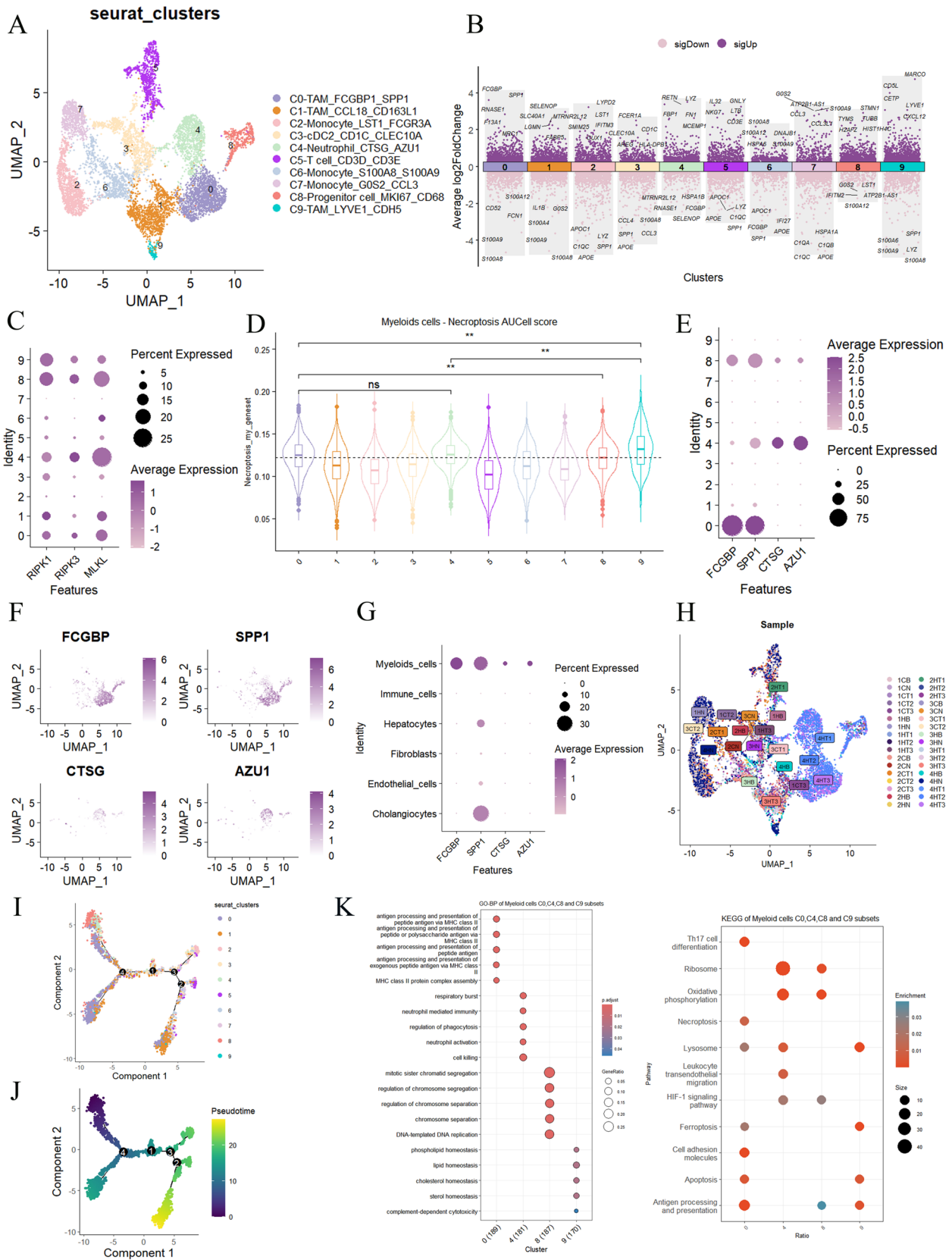


Fig 2 Necroptosis microlandscape of different subtypes of myeloid cells and pseudotime analysis. **A** All Myeloid cells were separated, followed by dimensionality reduction and clustering to obtain 10 subsets, which were named according to characteristic genes. **B** Volcano map of genes identified by 'FindAllMarkers' function, top5 up- and down-regulated marker genes of each subset were showed; sigDown: significantly down-regulated, sigUP: significantly up-regulated. **C** Expression of RIPK1, RIPK3 and MLKL in 10 subsets. **D** Violin plots of necroptosis scores of 10 subsets which were calculated by AUCell software (*, $P < 0.05$; **, $P < 0.01$; ***, $P < 0.001$; ****, $P < 0.0001$; ns, $P > 0.05$). **E** Expression of FCGBP, SPP1, CTSG and AZU1 in 10 subsets. **F** FCGBP, SPP1, CTSG and AZU1 were mainly concentrated in the C0 and C4 subsets of myeloid cells. **G** Expression of FCGBP, SPP1, CTSG and AZU1 in all cell types, also FCGBP, CTSG and AZU1 were detected only in myeloid cells. **H** The source information of all samples was mapped to the UMAP; C0 and C4 subsets were mainly from HCC_4 samples. **I** Pseudotime analysis predicted the evolutionary trajectories of 10 myeloid cell subsets. **J** Pseudotime analysis predicted sequential timing in evolutionary trajectories. **K** Functional enrichment analysis of genes in C0, C4, C8 and C9 subsets

that myeloid cells were the most predominant cell type that underwent necroptosis in PLC single-cell atlas, necroptosis microenvironment in PLC single-cell atlas was mainly constructed by myeloid cells.

The necroptosis microenvironment of various subtypes of myeloid cells in PLC

To further investigate the specific roles of myeloid cells in PLC necroptosis microenvironment, we separated all myeloid cells and re-executed dimensionality reduction clustering based on Seurat software, and a total of 10 cell subsets (C0–C9) were identified (Fig. 2A). The corresponding marker genes of C0–C9 subsets were identified by using the 'FindAllMarkers' function of COSG software and Seurat software, respectively (see Supplementary Material S5 for COSG results and 'FindAllMarkers' results). Based on marker genes identified by 'FindAllMarkers' function, volcanoes were mapped by using 'scRNAtoolVis' and top 5 up- and down-regulated marker genes of each subset were showed (Fig. 2B). C0–C9 subsets were identified by combining genes identified by COSG software and the 'FindAllMarkers' function with genes used to define different myeloid cell subtypes in published studies [24, 25]. Thus, not all genes used to define cell names are derived from marker genes identified by the 'FindAllMarkers' function (e.g., CTSG and AZU1 genes of C4 subsets are derived from the identification results of COSG software). In brief, we defined different myeloid cell subtypes in PLC by robust methodology, including TAM (C0, C1 and C9), monocytes (C2, C6 and C7), cDC2 (C3), neutrophils (C4), progenitor cells (C8); Since C5 subset highly expressed T cell marker genes (CD3D and CD3E), we speculated that dimensionality reduction and clustering of cell subsets by unsupervised clustering could not separate different cell types exactly, a small portion of T

cells were inevitably mixed in myeloid cells, but it did not affect our subsequent studies. We observed the expression of RIPK1, RIPK3 and MLKL in C0–C9 subsets (Fig. 2C), in which MLKL was mainly expressed in C0, C1, C4, C6, C8 and C9 subsets. Furthermore, we calculated necroptosis scores of C0–C9 subsets in the same way as before, among which the ranked top scores were C9, C0, C4 and C8 subsets (Fig. 2D). Considering the counts of different subsets, we concluded that C0-FCGBP1 + SPP1 + TAM and C4-CTSG + AZU1 + Neutrophils were most likely the cells that mainly underwent necroptosis in PLC. We then characterised the expression of FCGBP, SPP1, CTSG and AZU1 in C0–C9 subsets to determine their specificity (Fig. 2E). By mapping marker genes expression of C0 and C4 subsets to UMAP results, we confirmed that these genes were highly specific (Fig. 2F). We also confirmed that FCGBP, CTSG and AZU1 were specifically expressed in myeloid cells whereas absent in epithelial cells (Fig. 2G). Notably, we found that the C9, C0 and C4 subsets were mainly from samples 4HN, 4HT1, 4HT2 and 4HT3 (HT: HCC Tumor core) by mapping the sample source information to the UMAP (Fig. 2H). After examining tumor histological morphology in all samples using pathological HE section scan images, we discovered that HCC_4 samples (including 4HT1, 4HT2 and 4HT3) showed lower differentiation compared to HCC_1, HCC_2 and HCC_3 samples. Moreover, we also observed more single-cells necrosis or apoptosis in HCC_4 samples (see Supplementary Material S6 for HE images of HCC1–4 samples). Subsequently, we conducted pseudotime analysis on C0–C9 subsets (Fig. 2I–J), and found that C4 and C8 were early stage subsets with lower pseudotime value. Conversely, C0, C1, and C9 were terminal stage subsets, with higher pseudotime values, indicating potential spectral differentiation of myeloid cells. Due to the relatively high necroptosis scores observed in C0, C4, C8, and C9 subsets, we performed gene function enrichment analyses on these subsets separately (Fig. 2K). The marker genes in C4 subsets are primarily associated with the immune activation functions of neutrophils. The marker genes in C8 subsets are mainly related to chromosome segregation. The marker genes in C0 subsets are primarily linked to MHC class II antigen presentation. The marker genes in C9 subsets are mainly associated with lipid metabolism. Notably, the kegg enrichment analysis for C0 subsets included necroptosis, suggesting that C0 subsets may be more likely to undergo necroptosis compared to C4, C8, and C9 subsets. This is consistent with our previous speculation.

Co-localization of FCGBP + SPP1 + TAM in HCC spatially correlates with regions of poorer tumor differentiation

To investigate the spatial distribution of myeloid cell subsets that underwent necroptosis in PLC and to confirm potential interactions with tumor cells, we utilized Seurat

software to perform dimensionality reduction and clustering of HCC samples based on ST dataset [26]. As a result, a total of 12 subsets from H0–H11 were obtained (Fig. 3A), which were subsequently mapped to spatial image and paired with HE-stained images. Our findings showed that dimensionality reduction and clustering were able to distinguish various tumor regions effectively. Specifically, subsets H1, H9, and H11 were predominantly located in poorly differentiated tumor areas with significant stromal hyperplasia, whereas subsets H2, H7, and H10 were not (Fig. 3B). As each spot in ST generally contains several cells, the resolution of ST is not high enough to recognize the cell types contained in each spot compared to ScRNA-seq. To identify the cell types and proportions of cells that might be present in each HCC sample spot, we used SpaCET software. Furthermore, we utilized the dataset integrated into SpaCET software to identify malignant spots that are correlated with specific tumor types, as well as determine the percentage of malignant cells in the spots (Fig. 3C). The distribution of darker red points in the malignant result plot corresponds to more malignant spots, which is consistent with HE images, thus demonstrating the reliability of the SpaCET software. We also analyzed the proportion of macrophage M1, macrophage M2, endothelial cells, and cancer-associated fibroblasts (CAF) in each spot. Macrophage M2 and CAF had relatively higher proportions in areas with stromal hyperplasia (see Supplementary Material S7 for all identified cell types in each spot). Based on previous results in ScRNA-seq dataset, we mapped the expression of necroptosis-related genes (FCGBP, SPP1, CTSG and AZU1) in spatial HCC sample image, and found that myeloid cells with necroptosis were mostly involved in HCC with poorer differentiation. Although CTSG and AZU1 genes were hardly detected (see Supplementary Material S8), the spatial spot of FCGBP gene we detected was significantly co-localized with macrophage and poorer differentiated tumor regions (Fig. 3D). We also observed high SPP1 expression in HCC samples in the poorer tumor differentiation region, primarily in tumor cells. The expression of SPP1 in macrophages was not apparent in ST dataset, but several studies have shown that SPP1 indeed expresses in TAM [27]. In addition, macrophages were found to be co-localized with CAF in HCC, suggesting that there may be a potential interaction between them. Lastly, we examined the expression of the classical hepatocyte marker (ALB) and the classical cholangiocyte marker (KRT19) in HCC samples, and found that KRT19 was only expressed at a very low level in HCC samples, and found that the regions with relatively lower ALB expression are also the regions with poorer differentiation (Fig. 3D). Previous studies have shown that the poorer tumor differentiation is often associated with lower the degree of ALB expression in HCC [28, 29]. In

addition, we showed the expression of RIPK1, RIPK3, MLKL and CD68 (Fig. 3D), and we could see that the expression of MLKL and RIPK3 was low and mainly concentrated in poorly differentiated areas of the tumor. These results are consistent with our results that tumor regions with relatively lower ALB expression are also the regions with poorer differentiation. In conclusion, our findings suggest that FCGBP + SPP1 + TAM in HCC is spatially co-localized with poorer differentiated tumor regions.

FCGBP + SPP1 + TAM in iCCA co-localized spatially with the tumor region

To confirm the spatial localization of FCGBP + SPP1 + TAM in iCCA and explore its potential role, we applied the same method as before for dimensionality reduction and clustering of iCCA samples, producing 11 subsets from I0 to I10 (Fig. 4A). By mapping 11 subsets into spatial image plot (Fig. 4B) and combining with HE image, showed that I1, I3, I4, I7 and I9 subsets were mainly distributed within the tumor area. We also identified malignant spots in iCCA samples, as well as determined the proportion of possible cell types in each spot (Fig. 4C, Supplementary Material S7). Macrophage and CAF were found mainly in the paramalignant region and much less in tumor region. SPP1 and KRT19 were predominantly expressed in iCCA tumor tissues, while ALB was mainly expressed in hepatocytes in the paramalignant region (Fig. 4D). Interestingly, FCGBP expression in iCCA samples remained higher in tumor regions (Fig. 4D), significantly co-localizing with tumor tissue, and with a larger number of FCGBP -expressing spots compared to HCC samples. We also demonstrated the expression of RIPK1, RIPK3, MLKL and CD68, again revealing that the number of spots expressing RIPK3 and MLKL was significantly higher than in HCC (Fig. 4D). Previous studies administered transposable vectors pCaMIN (encoding Myc and NrasG12V) or pCaMIA (encoding Myc and AKT1) to mouse liver via hydrodynamic tail-vein (HDTV) injection and electroporation (Epo), respectively. These studies found that both HCC and iCCA induced by these two methods were derived from normal hepatocytes, and high expression of necroptosis-associated protein phosphorylated MLKL and RIPK3 was detected in the model induced into iCCA [21]. We found that the paramalignant region of iCCA also had a certain level of malignancy rather than completely normalcy (Fig. 4C), iCCA tumor regions with low expression rather than no expression of ALB suggested that they may have originated from hepatocytes. Therefore, we hypothesized that hepatocytes with low malignancy in paramalignant regions may progress into iCCA cancer cells if they are exposed to a necroptosis microenvironment.

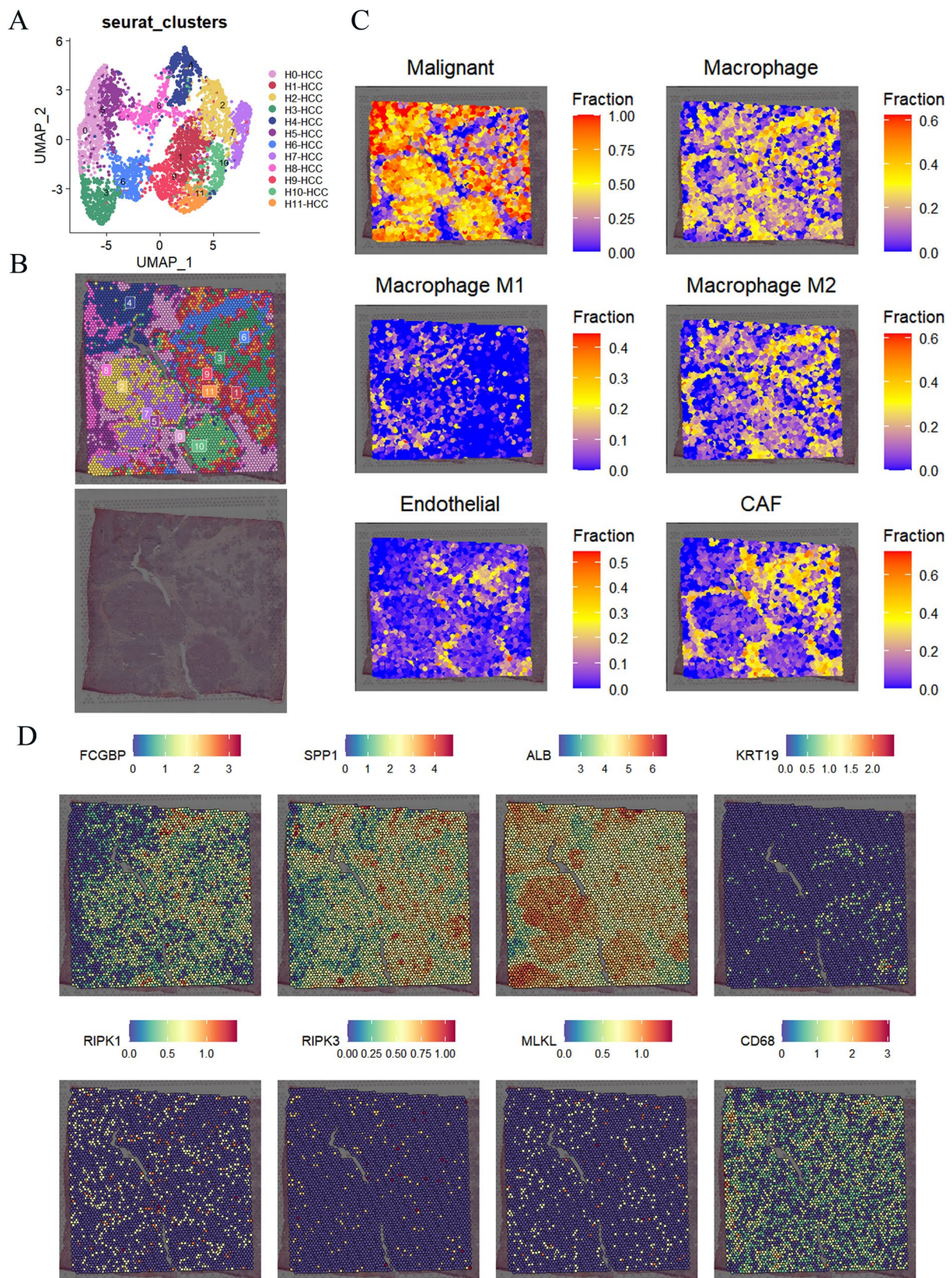


Fig 3 HCC ST analysis. **A** By dimensionality reduction and clustering of all Spots of HCC samples, a total of 12 subsets from H0 to H11 were obtained. **B** Spatial image and HE image of HCC samples. **C** SpaCET software identified the celltypes and the proportions cor-

responded in each spot, and also identified spots which were most likely to be malignant. **D** Spatial expression of FCGBP, SPP1, ALB, KRT19, RIPK1, RIPK3, MLKL and CD68 in HCC, with blue to red colours representing low to high expression

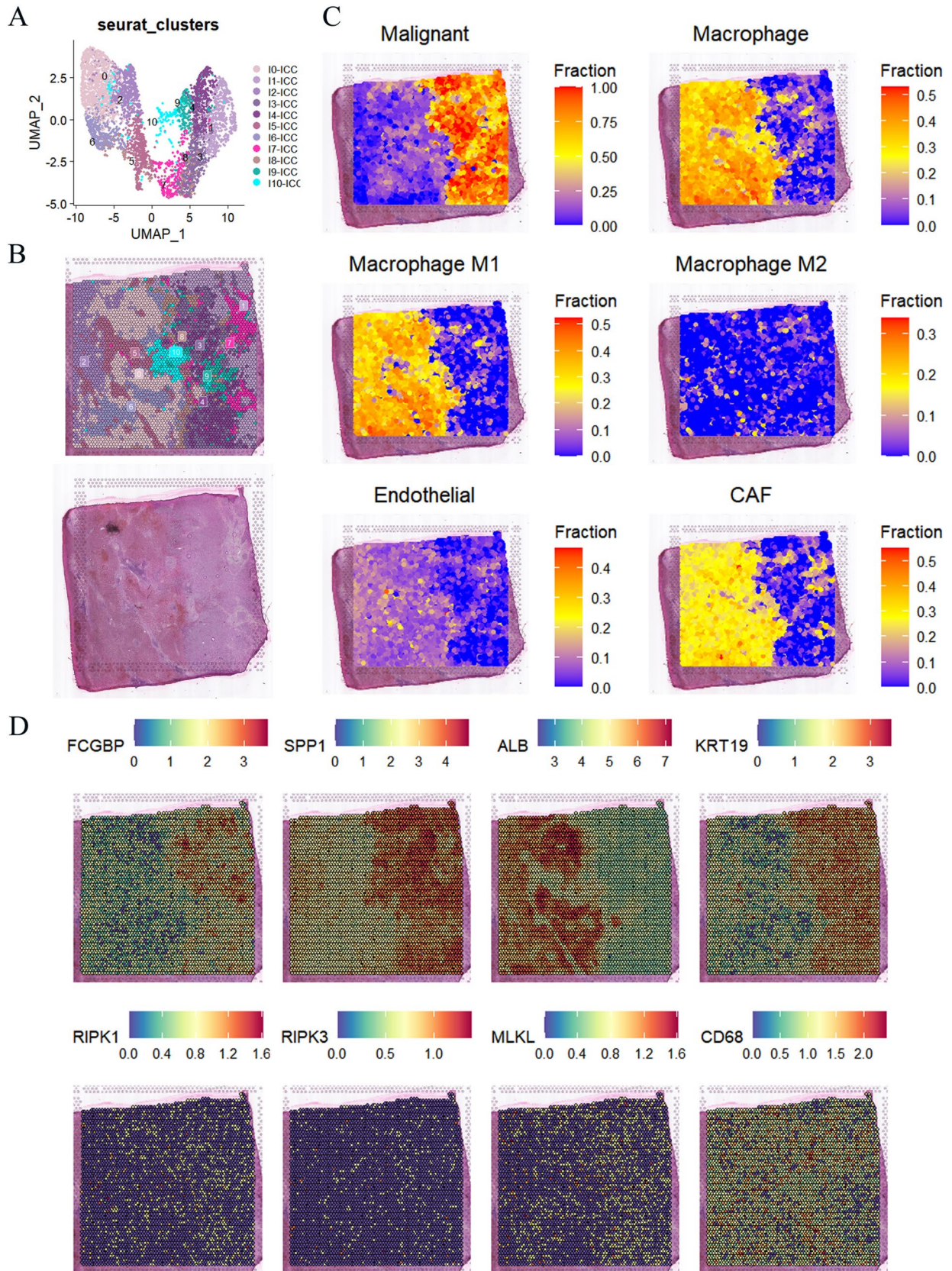


Fig 4 iCCA ST analysis. **A** Dimensionality reduction and clustering of all Spots in iCCA samples, a total of 11 subsets from I0 to I10 were obtained. **B** Spatial image and HE image of iCCA samples. **C** SpaCET software identified the celltypes and the corresponding proportions in each Spot, also identified Spots which were more likely to be malignant. Fraction ranging from 0 to 1 represents the percentage of corresponding celltypes in that Spot. **D** Spatial expression of FCGBP, SPP1, ALB, KRT19, RIPK1, RIPK3, MLKL and CD68 in iCCA, with blue to red colours representing low to high expression (Color figure online)

FCGBP + SPP1 + TAM promotes cHCC-CCA to gradually acquire the characteristics of iCCA

To advance our analysis, we explored the expression of FCGBP in cHCC-CCA samples from the ST dataset. Employing the same method as before, we completed dimensionality reduction and clustering for cHCC-CCA samples, which resulted in 13 cell subsets from C0 to C12 (Fig. 5A). The mapping of these subsets onto the spatial image, combined with HE image, revealed that subsets C0, C1, C2, C3, C7, C11, and C12 are primarily distributed in the tumor area (Fig. 5B). We used the same method to identify malignant spots and the proportion of macrophage M1, macrophage M2, endothelial, and cancer-associated fibroblasts (CAF) in each spot in cHCC-CCA samples (Fig. 5C, Supplementary Material S7). The region (defined as region 1) where C3 and C7 subsets located have more characteristics of iCCA (high expression of KRT19), while the region (defined as region 2) where C0 and C1 located have some characteristics of HCC (low expression of ALB, almost no expression of KRT19, Fig. 5D). Compared to region 2, FCGBP and SPP1 are concentrated in region 1 (Fig. 5D). We also showed the expression of RIPK1, RIPK3, MLKL and CD68 (Fig. 5D), and we found that the expression of RIPK3 and MLKL was more widely distributed, and the number of spots expressing RIPK3 and MLKL was still significantly higher than in HCC. It was found that the spatial distribution of FCGBP and SPP1 was roughly the same as that of macrophages (Fig. 5C), indicating that FCGBP + SPP1 + TAM was co-located with regions with more characteristics of iCCA. The necroptosis microenvironment induced by FCGBP + SPP1 + TAM may promote the progression of region 2 to region 1 in cHCC-CCA.

ScRNA-seq analysis of potential differentiation processes in PLC

To further investigate the mechanism underlying the transformation of premalignant cells to cHCC-CCA and iCCA, We extracted all epithelial cells in ScRNA-seq dataset and performed dimensionality reduction and clustering using Seurat software, resulting in a total of 8 cell subsets (C0-C7). According to the sample source information, the clustering

results of C0-C7 subsets in different cases and sample locations of HCC and iCCA were obtained (Fig. 6A–B). By mapping the sample origin information to the UMAP of all epithelial cells (Fig. 6C), we observed that the C4 subset was mainly derived from HCC_4 sample, while the C2 subset was mainly derived from HCC_1 sample. Examination of the morphology of tumor tissues in HE sections revealed that the HCC_4 sample exhibited less differentiation than the HCC_1 sample (see supplementary material S6). We predicted large-scale chromosome copy number variation (CNV) in all epithelial cells using inferCNV software. C1 subsets had almost no CNV; the remaining subsets all had varying degrees of CNV, implying that these subsets could be tumor cells or malignant precursor cells (Fig. 6D). We identified the characteristic genes of C0-C7 subsets by using 'FindAllMarkers' function of COSG software and Seurat software, respectively (The COSG and FindAllMarkers results are detailed in Supplementary Material S9). Based on marker genes identified by 'FindAllMarkers' function, volcano was mapped by using 'scRNAatoolVis' and top5 up- and down-regulated marker genes of each subset were showed (Fig. 6E). We carefully examined the marker genes of these subsets (Fig. 6F), and excluded C1 subset in subsequent studies because it highly expressed in fibrillar interstitial markers (VIM) and immune cell markers (CD3E), barely expressed ALB, and did not express KRT19. Then pseudotime analysis was performed on the remaining 7 subsets except for C1 subset (Fig. 6G–I). The results indicated that C0 and C6 subsets were in initial stage of potential lineage differentiation indicated by their lower pseudotime value in State 1. On the other hand, the C7 subset was situated towards the end of State 1 in an intermediate state, and was primarily derived from tumor core of HCC sample. It may be noted that the C2 subset was likely to be the terminal stage for further differentiation of malignant epithelial cells into higher malignant HCC epithelial cell lineage, with a higher pseudotime value in State 2. This subset showed high expression of EPCAM and APOA1, low expression of KRT19, hardly any expression of ALB. Regarding the C3 (EPCAM + KRT19 + SPP1-ALB-) and C5 (EPCAM + KRT19 + SPP1 + ALB+) subsets, they were mainly derived from iCCA samples, and there was a significant difference in SPP1 and ALB expressions between the two subsets. The C4 (EPCAM-KRT19-SPP1 + ALB+) subset was derived from relatively poorly differentiated HCC samples. Moreover, the C2 and C4 subsets appear to be at a fork in their potential lineage differentiation. The C4 subset expresses ALB and SPP1 but hardly expresses EPCAM, while C2 subset expresses EPCAM but hardly expresses ALB and SPP1. Importantly, both myeloid subsets with high scores of necroptosis (Fig. 2H) and tumor epithelial C4 subset were almost entirely from HCC_4 samples (Fig. 6C), indicating that the malignant epithelial C4 subset from HCC may have the potential to evolve further to

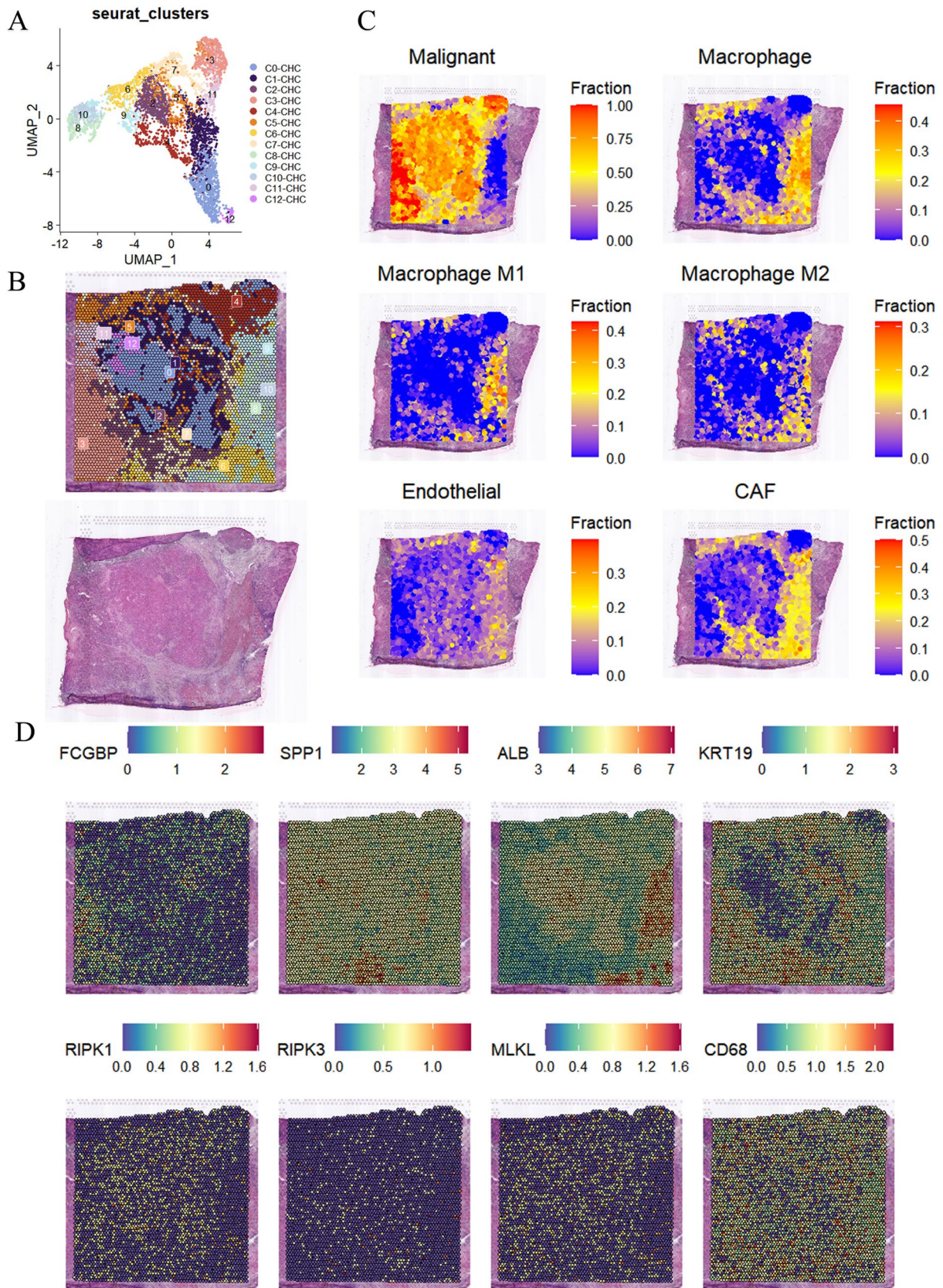


Fig 5 cHCC-CCA ST analysis. **A** Dimensionality reduction and clustering of all Spots in cHCC-CCA sample from ST dataset, a total of 13 subsets from C0 to C12 were obtained. **B** Spatial image and HE image of the cHCC-CCA sample. **C** SpaCET software identified the celltypes and the corresponding proportions in each Spot, also identified Spots which were more likely to be malignant. Fraction ranging from 0 to 1 represents the percentage of corresponding celltypes in that Spot. **D** Spatial expression of FCGBP, SPP1, ALB, KRT19, RIPK1, RIPK3, MLKL and CD68 in cHCC-CCA, respectively, with blue to red colours representing low to high expression

iCCA or HCC-CCA. This process is closely associated with the myeloid subsets involved in necroptosis.

Key switch genes associated with epithelial trajectory changes in a single-cell atlas of PLC

Potential switch genes of State1 to State2 and State1 to State3 progressions were screened by GeneSwitches software (Fig. 7A–B). The genes predicted to be switched on at mid-term of State1 to State2 progression include LY6K, EPCAM and ASCL2 genes, of which, EPCAM was a common epithelial SRG, while ASCL2 gene was also suggested to have an important role in dedifferentiation of intestinal epithelial cells to form small intestinal stem cells [30]. The genes predicted to be switched on at mid-term of State1 to State3 progression include S100A6, KRT7, KRT19, CLDN4 and others. The genes that were switched off at mid-term of State1 to State3 progression included lipid-related genes such as APOC1, APOA2 and APOE, which were not observed at mid-term of State1 to State2 progression, suggesting that the progression to iCCA or HCC-CCA was also related to lipid metabolism in pseudotime analysis. We observed gene changes by jitter plot, including ADH1B, CYP3A4, and several genes which were switched on in mid-term progression (KRT7, ASCL2, EPCAM, LY6K, CLDN4, KRT19 and S100A6) (Fig. 7C), and found that KRT7 was up-regulated during the evolution of epithelial C7 subset to epithelial C4 subset and further up-regulated during the differentiation of epithelial C4 subset to epithelial C3 subset, no similar changes were observed for KRT19. We observed the expression of KRT7, KRT19, S100A6 and EPCAM in all epithelial cells (Fig. 7D), and found that C4 subset partially expressed KRT7, C3 subset highly expressed S100A6, KRT7 and KRT19 as the terminal point of lineage progression, suggesting a possible important role of KRT7 in the progression of C4 subset to C3 subset. We checked the spatial distribution and expression of S100A6 in ST dataset, in which S100A6 grabbed our attention, the expression level of S100A6 from high to low was: tumor region in iCCA, region 1 in cHCC-CCA, region 2 in cHCC-CCA, more poorly differentiated region in HCC, and better differentiated region in HCC, which seems to indicate that the more iCCA features, the higher the expression of S100A6 (Fig. 7E). In the

ScRNA-seq dataset, C4 epithelial cells as the main subset constituting the early term of State3 highly expressed MET but not expressed EPCAM (Fig. 6D–E), whereas EPCAM was the gene predicted to be switched on in the progression of State1 to State2. We checked the spatial distribution of MET and EPCAM in the ST dataset (Fig. 7F), and found that MET gene was the most highly expressed in cHCC-CCA, followed by iCCA and then HCC. The MET + C4 subset was most likely to be observed in cHCC-CCA, especially in cHCC-CCA region 2. Coincidentally, region 2 of cHCC-CCA hardly expressed or minimally expressed EPCAM, while region 1 highly expressed EPCAM. Combined with the spatial distribution of cells with most probability of necroptosis in cHCC-CCA, it was suggested that the C4 subset of epithelial cells could be induced to iCCA and cHCC-CCA by necroptosis microenvironment. We also examined the immunohistochemical expression of S100A6 and the histological morphology features of 36 PLCs in the Human Protein Atlas (HPA) database, the results showed that S100A6 was detected in the tumor cells of 18 PLCs (including 15 cholangiocarcinomas and 3 hepatocellular carcinomas), but was not detected in the remaining PLCs (including 18 hepatocellular carcinomas). We found that only 3 of 21 HCC cases expressed S100A6, and the histomorphological features of these 3 HCC cases showed a strong inflammatory background, even with patches of necrotic areas while the HCCs tumor cells without such inflammatory background did not express S100A6. In order to comprehensively validate our findings, we performed immunohistochemistry: In HCC, well-differentiated tumor regions (HCC① and HCC②) showed low to no expression of S100A6. However, in tumor regions with a strong inflammatory background (HCC③ and HCC④), S100A6 expression was significantly enhanced, along with poorer tumor differentiation. In combined type cHCC-CCA, both tumor regions with hepatocellular carcinoma features and those with cholangiocarcinoma features exhibited strong S100A6 expression. Furthermore, tumor regions with cholangiocarcinoma features had even stronger S100A6 expression compared to those with hepatocellular carcinoma features. In mixed type cHCC-CCA and iCCA tumor regions, S100A6 expression was extremely high (Fig. 7G). This is consistent with our previous finding that HCC_4 samples have a severe inflammatory background in the ScRNA-seq dataset (Supplementary Material S6). In HCC_4 samples the myeloid cells had the highest score of necroptosis and the tumor cells were the C4 epithelial cell subset that might have the potential to differentiate toward iCCA or cHCC-CCA. Above results suggest us that the undergoing of necroptosis may be critically associated with the inflammatory background of PLC tumors, and the expression of S100A6 in HCC with a severe tumor inflammatory background suggests that it may have the potential to differential toward iCCA or cHCC-CCA.

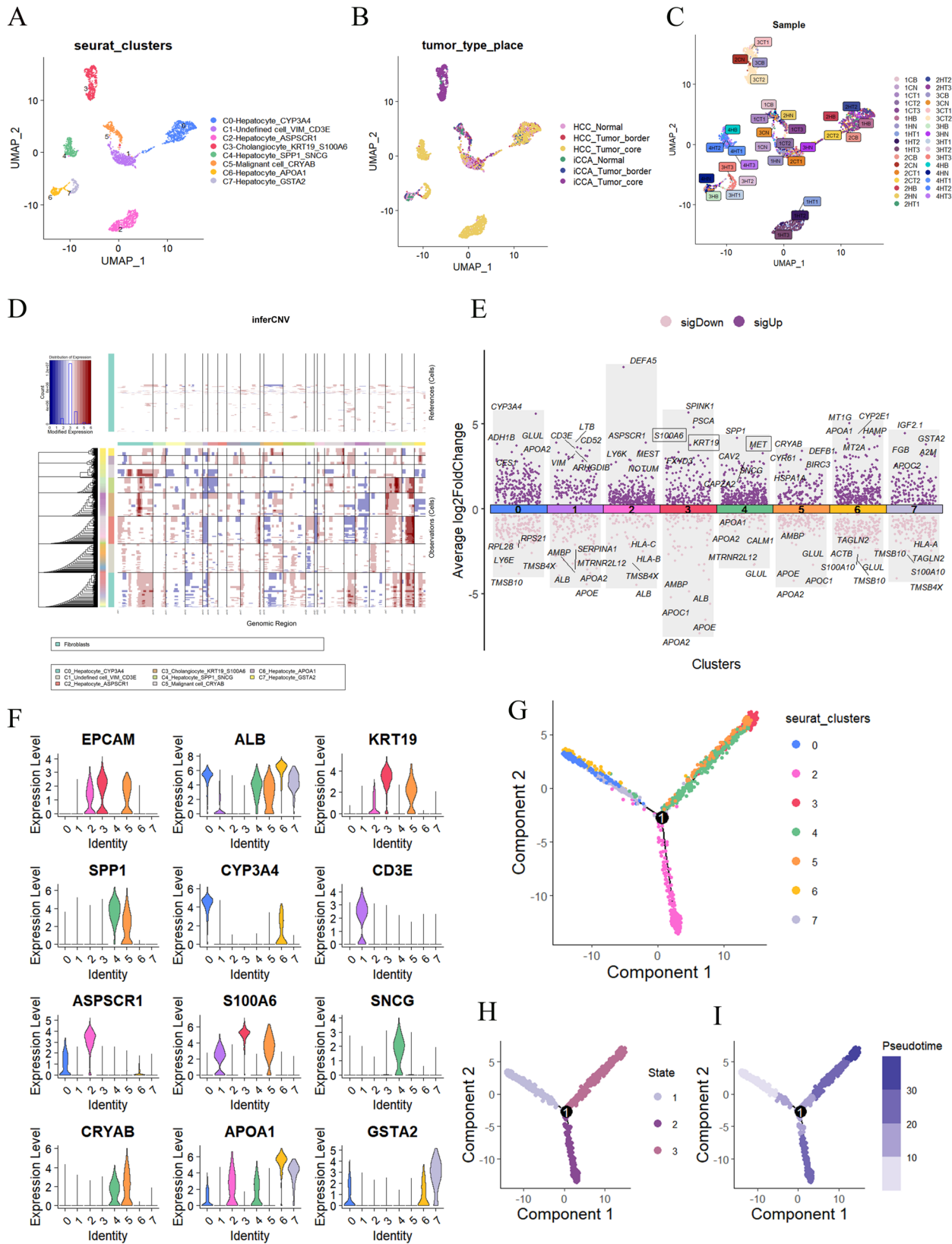


Fig 6 Pseudotime analysis of PLC epithelial cells. **A** All epithelial cells (including hepatocytes and cholangiocytes) in the scRNA-seq dataset were clustered to eight cell subsets from C0 to C7 by dimensionality reduction and clustering, and the cell subsets were named by their marker genes. **B** Sample source information was mapped to tumor type map. **C** Sample source information was mapped to UMAP. **D** Heatmap of CNV in epithelial cells based on scRNA-seq prediction (after noise reduction), red color indicates large-scale copy number amplification, blue color indicates large-scale copy number deletion, and the corresponding chromosomes are displayed on the top of the heatmap, the darker the color means the more significant the CNV is, and it is usually considered that the cells with large-scale CNV are tumor cells. **E** Volcano map of genes identified by 'FindAllMarkers' function, top5 up- and down-regulated marker genes of each subset were showed; sigDown: significantly down-regulated, sigUP: significantly up-regulated. **F** Violin plots of EPCAM, ALB, KRT19, SPP1 and several other cell subsets signature genes. **G** Cellular evolutionary trajectories predicted by pseudotime analysis of epithelial cells C0–C7 subsets (except C1 subset). **H** State variation of evolutionary trajectories predicted by pseudotime analysis. **I** Sequential timing of evolutionary trajectories predicted by Pseudotime analysis (Color figure online)

Immunofluorescence and immunohistochemistry reveals significant co-localization of CD68 and pMLKL in PLC

We collected FFPE sections from 3 cases of HCC, 1 case of iCCA and 2 cases of cHCC-CCA, totaling 6 cases. The cancer tissues of HCC1 and HCC2 samples were poorly differentiated, with more noticeable necrosis observed. In contrast, the cancer tissue of HCC3 sample was relatively well-differentiated with no obvious necrotic areas observed (Supplementary Material S10). In our previous single-cell transcriptomic results, we found that necroptosis cell death mainly occurred in FCGBP + SPP1 + myeloid cells. Furthermore, we demonstrated in spatial transcriptomic results that FCGBP + SPP1 + TAMs were spatially co-localized with poorly differentiated tumor regions in HCC and cholangiocarcinoma-featured regions in iCCA and cHCC-CCA. We confirmed the subcellular localization of FCGBP, SPP1, MLKL and CD68 proteins on the genecards website [31]. FCGBP protein is a secreted protein, mainly present in exosomes. Our previous single-cell and spatial transcriptomic results also showed that in PLC, SPP1 expression in tumor cells was much higher than that in myeloid cells. Therefore, we did not perform immunofluorescence experiments for FCGBP and SPP1 proteins. As a major executor of necroptosis, MLKL protein can indicate cells that have undergone necroptosis at the protein level. Next, we performed immunofluorescence experiments for pMLKL and CD68 on these 6 cases (Fig. 8A), co-localization of pMLKL and CD68 was observed in HCC1, HCC2, iCCA, cHCC-CCA1 and cHCC-CCA2 samples. The most extensive co-localization of pMLKL and CD68 was observed in cHCC-CCA2 samples, while only a small number of pMLKL and CD68 co-localizations were visible in HCC1, HCC2, iCCA

and cHCC-CCA1 samples. No significant co-localization was observed in the well-differentiated HCC3 sample. To further prove our findings, we also conducted immunohistochemical staining for MLKL, SPP1, FCGBP and CD68 in 3 cases of HCC, 2 cases of iCCA, 2 cases of combined type cHCC-CCA and 2 cases of mixed type cHCC-CCA (Fig. 8B). The results showed that a small number of macrophages undergoing necroptosis could be observed in the HCC tumor region with a heavier inflammatory background, while the cancerous tissues in this region were relatively poorer differentiated; slightly more macrophages undergoing necroptosis were observed in iCCA cases; In combined type cHCC-CCA cases, macrophages undergoing necroptosis were more likely to be observed in areas with features of cholangiocarcinoma relative to areas with features of hepatocellular carcinoma; in mixed type cHCC-CCA cases, macrophages undergoing necroptosis were also easily observed.

Necroptosis-related myeloid cell communication with PLC epithelial cells

Our previous results suggested that C0-FCGBP + SPP1 + TAMs may be the main cell type undergoing necroptosis in PLC. To further explore the potential interactions between C0-FCGBP + SPP1 + TAMs, C4-CTSG + AZU1 + Neutrophils and PLC epithelial cells, we conducted cell communication analysis in the scRNA-seq dataset among C0-FCGBP + SPP1 + TAMs, C4-CTSG + AZU1 + Neutrophils and epithelial cells. A heatmap displaying the strength of cell communication between different cell subsets is shown (Fig. 9A). We found that nearly all epithelial cells, when serving as signal senders, exhibited varying degrees of cell communication with C0-TAM and C4-Neutrophils. Our previous results indicated that C4-Hepatocytes originate from the HCC_4 sample, and C0-TAMs and C4-Neutrophils undergoing necroptosis are predominantly from the HCC_4 sample. Pseudotime analysis also suggested that C4-Hepatocytes might progress into tumor cells with cholangiocarcinoma features. When C4-Hepatocytes served as signal senders, the strength of cell communication with C0-TAM and C4-Neutrophils was relatively higher compared to other epithelial cells, which piqued our interest. Subsequently, we highlighted three signal pathways with stronger communication intensity between C4-Hepatocytes, C0-TAMs and C4-Neutrophils (Fig. 9B–D), including SPP1 signaling, APP signaling and MIF signaling. It's worth noting that SPP1 signaling was not detected between C2-Hepatocytes, C0-TAMs and C4-Neutrophils, while MIF signaling exhibited the highest communication intensity among these cell types. We then focused on SPP1 signaling and APP signaling, visualizing the specifics of these

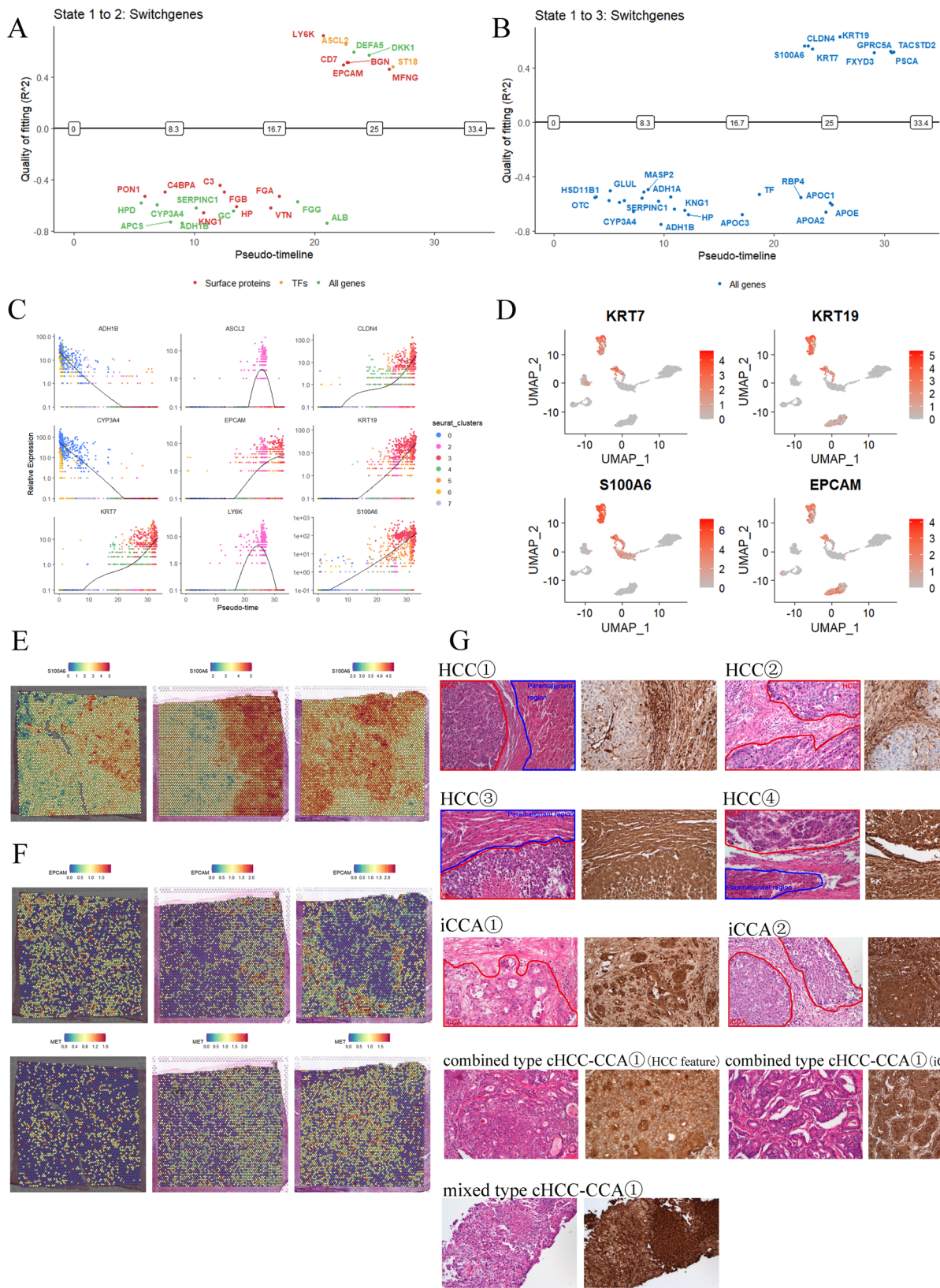


Fig 7 Analysis of switchgenes based on the results of the pseudotime analysis. **A–B** The software 'GeneSwitches' was used to predict the switchgenes of State1 to State2 and State1 to State3 respectively, and these switchgenes were identified as cell surface proteins and transcription factors according to the software, all genes indicated that the gene may be both a cell surface protein and a transcription factor. **C** Jitter plot of some key switchgenes. **D** Expression of KRT7, KRT19, S100A6 and EPCAM in epithelial C0–C7 subsets. **E–F** Spatial distribution and expression of S100A6, EPCAM and MET in ST dataset. **G** Immunohistochemical staining of S100A6 in HCC with a severe inflammatory background, HCC without an inflammatory background and cholangiocarcinoma. S100A6 was positively expressed in HCC tumor cells with a severe inflammatory background, negatively expressed in HCC tumor cells without an inflammatory background, and diffusely and strongly expressed in iCCA tumor cells (cancer tissue is labeled in red and the paramalignant region is labeled in blue; the paramalignant region consists mainly of hepatocytes and a few inflammatory cells)

pathways through a hierarchical plot. The left half of the hierarchical plot illustrates the reception of autocrine and paracrine signals by the specified cell groups (including C4-Hepatocytes, C0-TAMs and C4-Neutrophils). The right half shows the reception of autocrine and paracrine signals by the remaining cell groups in the dataset, with thicker lines indicating stronger communication intensity. When C4-Hepatocytes served as signal sources, they primarily communicated with C0-TAMs and C4-Neutrophils by secreting APP (Amyloid Beta Precursor Protein) in a paracrine manner (Fig. 9E). In contrast, SPP1 exhibited both strong autocrine and paracrine communication forms between C0-TAMs and C4-Hepatocytes (Fig. 9E), but the communication intensity of SPP1 between C4-Neutrophils and C4-Hepatocytes was relatively low. Although each spot in the ST data contained multiple cells, we still performed cell communication analysis on the data (see all cell communication results of ST data in Supplementary Material S11). We focused on the cell communication between FCGBP-high expression clusters and other clusters mentioned in previous results. In the spatial maps and corresponding circle plots, the thickness of lines represents the strength of signals. Results showed SPP1 still had the highest cell communication intensity and confidence among these clusters (Fig. 9F). In HCC-ST data, FCGBP-high clusters included H1, H6, H9 and H11. In ICC-ST data, FCGBP-high clusters included I3, I4, I7 and I9. In CHC-ST data, the FCGBP-high cluster was C1, C3, C7 and C11. Notably, cell communication of autocrine signals in ST data could also be between different cell types within the same spot, including communication between FCGBP + myeloid cells and tumor cells. However, combined with cell communication analysis in single cell datasets, it was clear that SPP1 cell communication played an important role in PLC, and was likely one way tumor cells regulated necroptosis cell death of myeloid cells.

Discussion

Dixit and Kayagaki first discovered through large-scale genetic experiments that knockdown of the gene encoding the dual transmembrane protein NINJ1 resulted in macrophages exhibiting impaired plasma membrane rupture (PMR) in response to diverse inducers of pyroptotic, necrotic and apoptotic cell death, as well as inability to release numerous intracellular proteins including HMGB1 (damage-associated molecular patterns, DAMPs) and LDH (a standard measure of PMR), which overthrew the long-held idea that cell death-related PMR is a passive event [32]. Recently, Hiller and Degen, using techniques such as super-resolution microscopy and cryoelectron microscopy, observed that NINJ1 was activated and bound together in the cell membranes of cells that have undergone programmed death. As more and more NINJ1 activated and thus formed larger aggregates, it eventually led to cell membrane cleavage [33]. Susana L Orozco et al. demonstrated that cells undergoing necroptosis were still able to produce cytokines through transcription and translation during the period from plasma membrane damage to final death [20]. These results suggested that cells undergoing necroptosis may not die immediately, and cells expressing MLKL may be in a period of unfinished cell membrane rupture. Therefore, the expression of MLKL cannot indicate cells that are about to undergo necroptosis or have already completed cell membrane rupture, thus the possibility of cell necroptosis needs to be assessed in combination with other related genes alterations. In our study, we analyzed the possible role of necroptosis in the progression of PLC using ScRNA-seq and ST datasets. By ScRNA-seq analysis, we found that FCGBP + SPP1 + TAM were the cells most likely to undergo necroptosis. By using ST dataset containing HCC, iCCA and cHCC-CCA, we demonstrated the presence of FCGBP + macrophages and their spatial co-location with poorer differentiated tumor regions in HCC, cholangiocarcinoma regions in iCCA and regions with more cholangiocarcinoma features in cHCC-CCA. In the absence of necroptosis microenvironment, pre-malignant cells could evolve into higher malignant HCC subtype, acquiring partial expression of SRG (e.g. EPCAM) and gradually losing ALB expression. When necroptosis underwent in FCGBP + macrophages to induce necroptosis microenvironment, pre-malignant cells evolve into iCCA with expression of S100A6, KRT7, KRT19 and EPCAM; on the other hand, pre-malignant cells could also evolve into tumor epithelial cells that retained part of characteristics of HCC (high expression of MET and S100A6, while low expression of ALB, hardly expression of KRT19 and EPCAM) and then develop into tumor cells with more iCCA characteristics (enhanced expression of KRT19 and

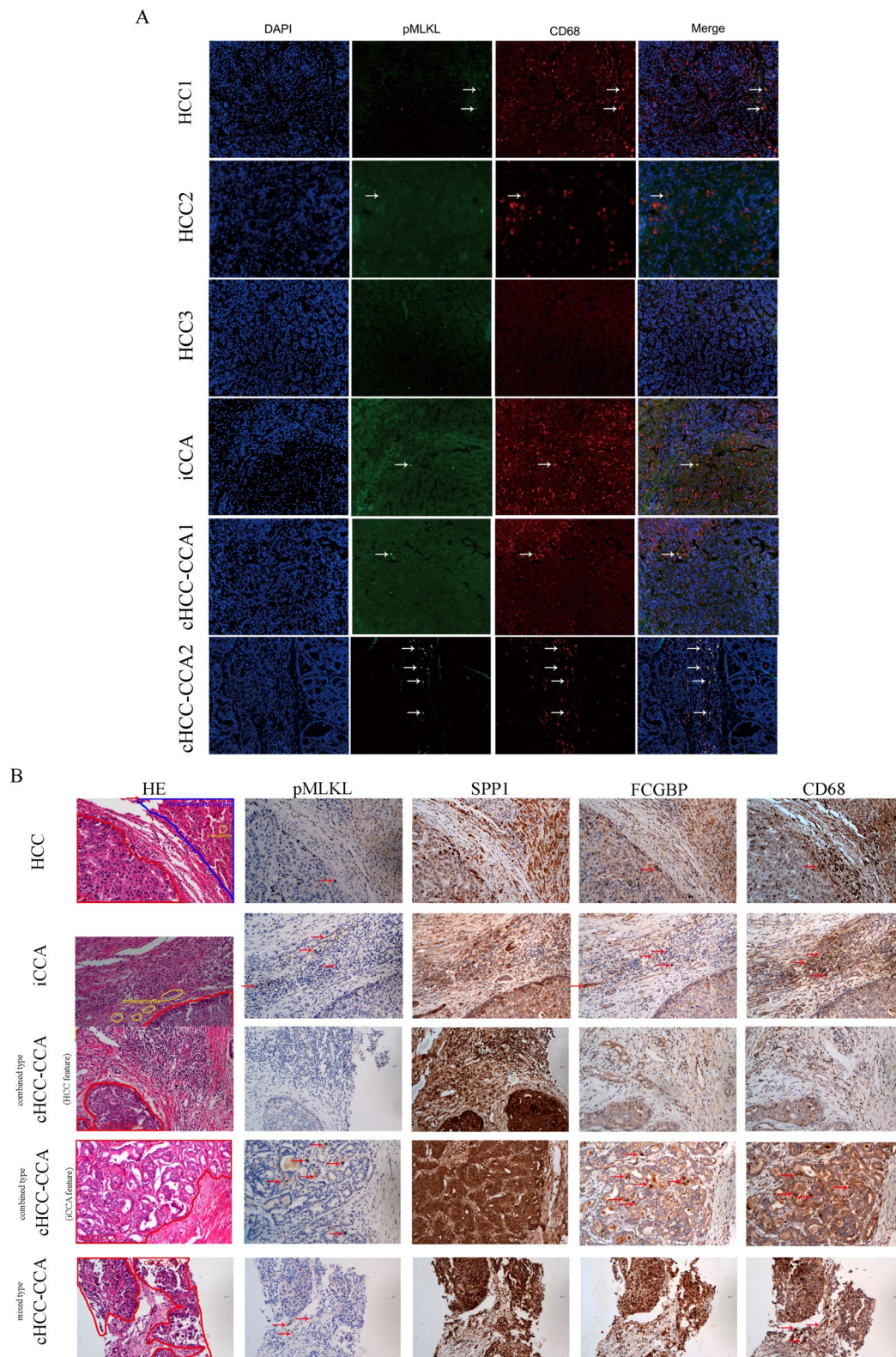


Fig. 8 Immunofluorescence staining and immunohistochemical staining. **A** Immunofluorescence experiments for pMLKL and CD68 in the 6 cases. Co-localization of pMLKL and CD68 was observed in HCC1, HCC2, iCCA, CHC1 and CHC2 samples. pMLKL: phosphorylated MLKL, representing the terminal event of necroptosis and indicating cells that have undergone necroptosis cell death; CD68

staining positive here indicates macrophages. **B** Immunohistochemical staining of MLKL, SPP1, FCGBP and CD68 (cancer tissue is labeled in red, paramalignant region in blue, and cholangiocytes in yellow; the paramalignant region consists mainly of hepatocytes and a few inflammatory cells) (Color figure online)

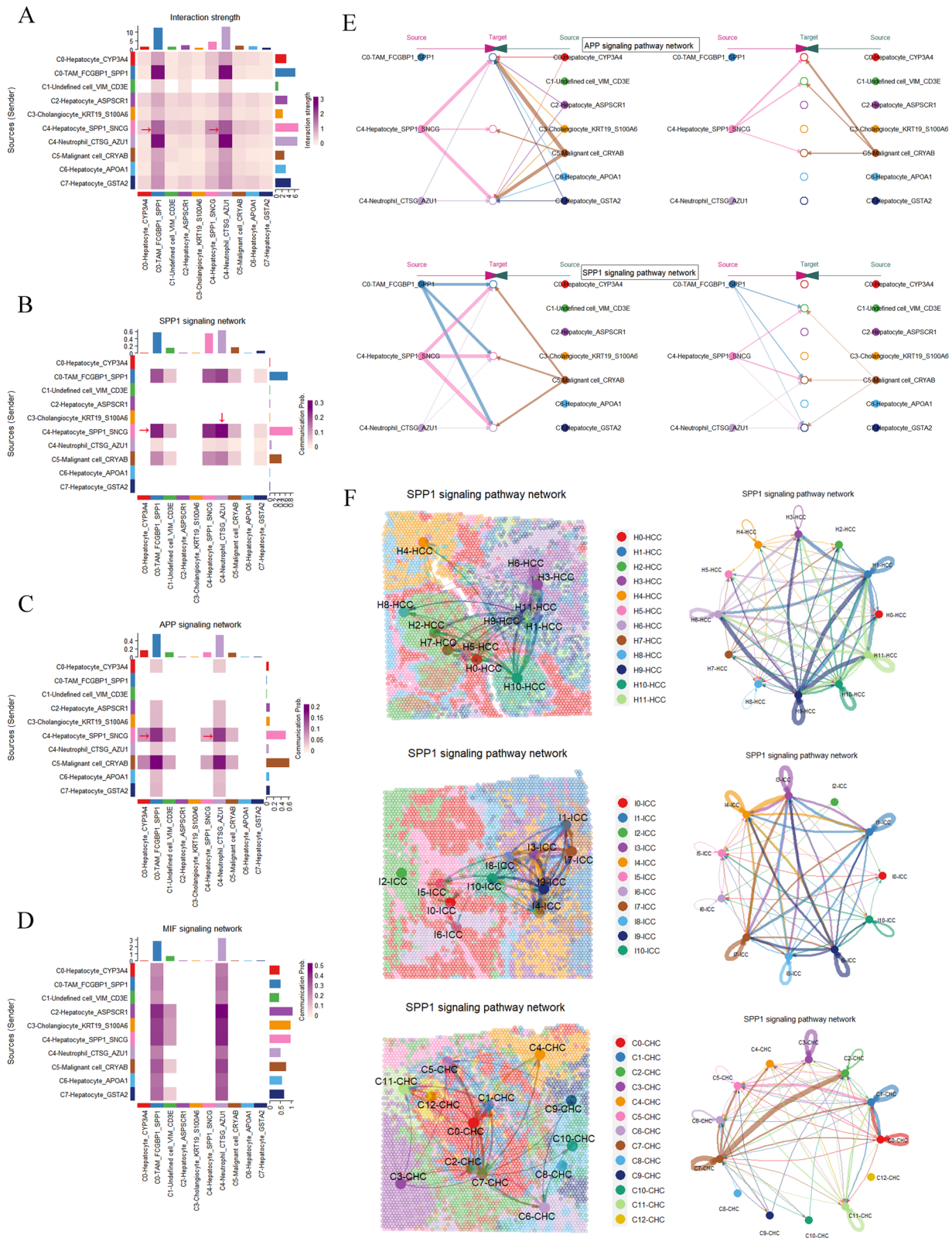


Fig 9 Cellchat Analysis in ScRNA-seq and ST datasets. **A** Heatmap of signal strength of communication between different cell subsets. **B** Heatmap of signal strength of SPP1 communication between different cell subsets. **C** Heatmap of signal strength of APP communication between different cell subsets. **D** Heatmap of signal strength of MIF

communication between different cell subsets. **E** Hierarchical plot visualizing the reception of autocrine and paracrine APP and SPP1 signals when C4-Hepatocyte, C0-TAM and C4-Neutrophil were the indicated cells. **F** Spatial image and corresponding circle plots, the thickness of lines represents the strength of signals

EPCAM, while reduced expression of ALB), which was similar to cHCC-CCA gene features. There were inconsistent studies on whether the survival rate of cHCC-CCA was worse than that of iCCA, but it was generally accepted that the survival rate of cHCC-CCA was worse than that of HCC. cHCC-CCA with HCC composition more than 70% had better overall survival (OS) than cHCC-CCAs with HCC composition less than 70%. The proportion of HCC or CCA components could predict cHCC-CCA patients' prognosis [34]. Based on our findings above, a dimensionality reduction of CCA proportion by inhibiting necroptosis microenvironment may have improved the prognosis of patients with cHCC-CCA.

In previous studies, tumor-associated macrophage (TAM) had been defined mainly as M1 macrophages and M2 macrophages. M1 macrophages were thought to have a pro-inflammatory response and anti-tumor effects, M2 macrophages were thought to promote cancer progression as well as inhibit the inflammatory response [35]. With the development of single-cell transcriptomics, tumor-associated macrophages were no longer simply defined as M1 and M2 macrophages. Further, studies had shown that in HCC, SPP1 + macrophages near the tumor boundary interacted with CAF to stimulate extracellular matrix remodeling and promoted the formation of tumor immune barrier (TIB) structure, which may have restricted immune infiltration of the tumor core. Blocking SPP1 or macrophage-specific deletion of *Spp1* in mice could destroy the TIB structure and sensitize HCC cells to immunotherapy, accompanied by a decrease in CAF and an increase in cytotoxic T cell infiltration [27]. In another study on breast cancer, macrophages with high expression of CD163, SPP1 and C1QC were defined as lipid-associated macrophages (LAM), distributed at the tumor-adipose junction, LAMs depletion in the tumor-adipose microenvironment (TAME) synergized the antitumor effects of anti-PD1 therapy [36]. Both of the above studies suggested that the presence of SPP1 + macrophages was associated with blocked immune cell infiltration and ineffective immunotherapy, which could be improved by inhibiting macrophage function through the SPP1 therapeutic target. In our study, we found that macrophages undergoing necroptosis expressed SPP1 and FCGBP, thus therapies targets SPP1 and FCGBP may inhibit the necroptosis of macrophages. There were few reports on FCGBP before. For the first time we reported that FCGBP was uniquely expressed in myeloid cells but hardly expressed in epithelial cells and other immune cells of PLC. It is highly likely that myeloid cells expressing FCGBP are the subtype of cells that mainly undergo necroptosis in PLC, which is critically related to necroptosis microenvironment. FCGBP may be a promising target for PLC immunotherapy, and further research is necessary in the future.

We were unable to strictly distinguish M1 macrophages, M2 macrophages and FCGBP + SPP1 + TAM, which are distinguished by different definitional models. Our study focused on analyzing the effect of necroptosis microenvironment induced by FCGBP + SPP1 + TAM in PLC on tumor progression. In addition, previous studies have reported the presence of TAMs at all stages of liver cancer progression, and destruction or re-differentiation of TAMs may be a viable therapeutic strategy for patients with liver cancer, which is mainly divided into three approaches: eliminate the production of M2 TAMs, remodel M2 TAMs to M1 TAMs and block the communication between M2 TAMs and liver cancer cells [37]. A study reported that SPON2 promotes M1-like macrophage recruitment and inhibits HCC metastasis through various Integrin-Rho GTPase-Hippo pathways [38]. However, another study reported that M1 macrophages induced expression of PD-L1 in HCC cells, supporting the pro-tumor role of M1 macrophages [39]. M1 and M2 macrophage functions may not always be mutually exclusive, but rather the two types of TAM are often co-occurring in the tumor microenvironment, and the two types of TAM cannot be considered completely distinct macrophage subtypes [38].

Due to the specificity of the ST data, we were unable to classify the different macrophage subsets with the same precision as the ScRNA-seq dataset. Therefore, we combined the properties of the ST data and ScRNA-seq data to analyze the potential role of macrophages in PLC tumor cell progression from different perspectives. The distribution of M1 and M2 macrophages predicted by the SpaCET software was noteworthy across the three cases examined. In the HCC sample of the ST dataset, the proportion of infiltrating M2 macrophages in the tumor region appeared higher than the proportion of M1 macrophages. Conversely, in the iCCA sample, the proportion of infiltrating M1 macrophages seemed higher than M2 macrophages in both the paraneoplastic and tumor regions; In cHCC-CCA sample of ST dataset, the distribution of M1 macrophages and M2 macrophages appeared to be little different in tumor region. In summary, in this ST dataset, the HCC sample were predominantly infiltrated with M2 macrophages in tumor paracancer and tumor core, while the iCCA and cHCC-CCA samples were predominantly infiltrated with M1 macrophages in tumor paracancerous regions. We hypothesize that M1 macrophages may promote a strong inflammatory response and be one of the reasons for further inducing necroptosis in FCGBP + SPP1 + TAM. This finding is consistent with our finding in the ScRNA-seq dataset that HCC_4 sample with the most severe inflammatory background were also the main source of the myeloid cells subsets with the highest necroptosis score, the pseudotime analysis results also suggested that epithelial C4 subset from HCC_4 sample

may have the potential to differentiate towards iCCA or cHCC-CCA.

Furthermore, switch gene analysis revealed that S100A6 played an important indicative role in the progression of different PLC tumor subtypes. Immunohistochemistry demonstrated that S100A6 was expressed in cancer cells in HCC cases with severe inflammatory backgrounds and all CCA cases. However, S100A6 was not expressed in HCC cases without inflammatory backgrounds, suggesting the inflammatory response had an important role in PLC tumor progression.

There were some limitations in our study. First, the lack of cHCC-CCA samples in our recruited ScRNA-seq dataset may have led to defective results from the pseudo-time analysis of epithelial cells. Second, the small number of sample cases in the recruited ST dataset may not have completely represented all PLC subtypes. Third, due to the data characteristics of RNA-Seq and ST, we could not perform a more rigorous classification of macrophage subtypes, which fortunately did not affect our findings. The FCGBP + SPP1 + TAM defined in the ScRNA-seq dataset was also observed in the ST dataset, although it did not correspond well to M1 or M2 macrophages. In summary, our study was based on robust bioinformatics analysis, and some results were validated by immunohistochemistry and immunofluorescence. However, additional functional experiments and cohort studies are still needed to validate the biological results and potential molecular mechanisms.

Conclusion

In conclusion, the cells undergoing necroptosis in PLC were principally the FCGBP + SPP1 + TAM, which co-localized with poorer differentiated region in HCC, iCCA tumor region and region with more cholangiocarcinoma characteristics in cHCC-CCA. The necroptosis microenvironment induced by necroptosis occurring in FCGBP + SPP1 + TAM may promote the progression of premalignant cells into iCCA and the acquisition of cholangiocarcinoma characteristics by cancer cells in cHCC-CCA. It may also participate in resistance to immunotherapy. Leveraging our extensive pathology diagnosis experience and robust bioinformatics analysis, we have for the first time innovatively explored the pivotal role of the tumor microenvironment in PLC progression, through a comprehensive assessment of gene sets with single-cell resolution. Furthermore, by utilizing both ScRNA-seq and ST datasets, we demonstrated the critical relationship between FCGBP + TAM and the necroptosis microenvironment. The integration of robust bioinformatics analysis and extensive pathology diagnosis experience bolstered the credibility of our study.

Supplementary Information The online version contains supplementary material available at <https://doi.org/10.1007/s10495-023-01908-3>.

Acknowledgements We thank all the team members for their hard work and efforts.

Author contributions CW designed and directed the study and wrote the manuscript. JC designed the study, performed the bioinformatics analysis and data generation, and wrote the original manuscript. WH was responsible for immunofluorescence experiment. LT and CC participated in writing review, editing, and funding acquisition. All authors read and approved the final manuscript.

Funding This study is supported by Shenzhen Science and Technology Program (Grant No. JSGG20201102162802008) and the Key Program for Clinical Research at Peking University Shenzhen Hospital (LCYJZD2021007).

Data availability The ScRNA-seq datasets generated during the current study are available in the GEO database (<https://www.ncbi.nlm.nih.gov/geo/query/acc.cgi?acc=GSE189903>). The ST datasets generated during the current study are available in the Genome Sequence Archive database (<https://ngdc.cncb.ac.cn/gsa-human/browse/HRA000437>).

Declarations

Conflict of interest The authors declare that they have no competing interests.

Ethics approval and consent to participate The samples used to perform the Immunofluorescence and immunohistochemistry were obtained from patients who gave informed consent and signed an informed consent form. The study was approved by the Ethical Review Committee of Peking University Shenzhen Hospital (PKUSZH)) (Approval Number: 2023115), and all experiments were performed in accordance with the Declaration of Helsinki ethical guidelines.

Consent for publication The authors declare that they have no competing interests.

References

1. Bray F, Ferlay J, Soerjomataram I, Siegel RL et al (2018) Global cancer statistics 2018: GLOBOCAN estimates of incidence and mortality. *CA Cancer J Clin* 68(6):394–424
2. Marquardt JU, Andersen JB, Thorgeirsson SS (2015) Functional and genetic deconstruction of the cellular origin in liver cancer. *Nat Rev Cancer* 15(11):653–667
3. Xue R, Chen LU, Zhang C et al (2019) Genomic and transcriptomic profiling of combined hepatocellular and intrahepatic cholangiocarcinoma reveals distinct molecular subtypes. *Cancer Cell* 35(6):932–947
4. Liu Y, Zhuo S, Zhou Y, Ma L et al (2022) Yap-Sox9 signaling determines hepatocyte plasticity and lineage-specific. *J Hepatol* 76(3):652–664
5. Fan B, Malato Y, Calvisi DF, Naqvi S et al (2012) Cholangiocarcinomas can originate from hepatocytes in mice. *J Clin Invest* 122(8):2911–2915
6. Sekiya S, Suzuki A (2012) Intrahepatic cholangiocarcinoma can arise from Notch-mediated conversion of. *J Clin Invest* 122(11):3914–3918

7. Wang J, Wang H, Peters M, Ding N et al (2019) Loss of Fbxw7 synergizes with activated Akt signaling to promote c-Myc dependent. *J Hepatol* 71(4):742–752
8. Hill MA, Alexander WB, Guo B et al (2018) Kras and Tp53 mutations cause cholangiocyte- and hepatocyte-derived cholangiocarcinoma. *Cancer Res* 78(16):4445–4451
9. Brunt E, Aishima S, Clavien PA, Fowler K et al (2018) cHCC-CCA: Consensus terminology for primary liver carcinomas with both. *Hepatology* 68(1):113–126
10. Guo Y, Long J, Lei S (2019) Promoter methylation as biomarkers for diagnosis of melanoma: a systematic review and meta-analysis. *J Cell Physiol* 234(5):7356–7367
11. Li L, Che L, Tharp KM, Park HM et al (2016) Differential requirement for de novo lipogenesis in cholangiocarcinoma and. *Hepatology* 63(6):1900–1913
12. Carlson CM, Frandsen JL, Kirchoff N, McIvor RS et al (2005) Somatic integration of an oncogene-harboring sleeping beauty transposon models. *Proc Natl Acad Sci U S A* 102(47):17059–17064
13. Chang Y, Jeong SW, Young Jang J, Jae Kim Y (2020) Recent updates of transarterial chemoembolization in hepatocellular carcinoma. *Int J Mol Sci* 21(21):8165
14. Louis DN, Perry A, Reifenberger G et al (2016) The 2016 World Health Organization classification of tumors of the central nervous system: a summary. *Acta Neuropathol* 131:803–820
15. Degterev A, Huang Z, Boyce M, Li Y et al (2005) Chemical inhibitor of nonapoptotic cell death with therapeutic potential for. *Nat Chem Biol* 1(2):112–119
16. Sprooten J, De Wijngaert P et al (2020) Necroptosis in immunology and cancer immunotherapy. *Cells* 9(8):1823
17. Yan J, Wan P, Choksi S, Liu ZG (2022) Necroptosis and tumor progression. *Trends Cancer* 8(1):21–27
18. Dhuriya YK, Sharma D (2018) Necroptosis: a regulated inflammatory mode of cell death. *J Neuroinflammation* 15(1):1–9
19. Wang H, Sun L, Su L, Rizo J et al (2014) Mixed lineage kinase domain-like protein MLKL causes necrotic membrane disruption. *Mol Cell* 54(1):133–146
20. Orozco SL, Daniels BP, Yatim N, Messmer MN et al (2019) RIPK3 activation leads to cytokine synthesis that continues after loss of cell. *Cell Rep* 28(9):2275–2287
21. Seehawer M, Heinzmann F et al (2018) Necroptosis microenvironment directs lineage commitment in liver cancer. *Nature* 562(7725):69–75
22. Nagtegaal ID, Odze RD, Klimstra D, Paradis V et al (2020) The 2019 WHO classification of tumours of the digestive system. *Histopathology* 76(2):182–188
23. Ma L, Heinrich S, Wang L et al (2022) Multiregional single-cell dissection of tumor and immune cells reveals stable lock-and-key features in liver cancer. *Nat Commun* 13(1):7533
24. Chu X, Zhang Y, Cheng S (2022) Heterogeneity of tumor-infiltrating myeloid cells in era of single-cell genomics. *Chin J Cancer Res* 34(6):543–553
25. Park JW, Kang J et al (2021) The prognostic significance of p16 expression pattern in diffuse gliomas. *J Pathol Trans Med* 55(2):102–111
26. Wu R, Guo W, Qiu X et al (2021) Comprehensive analysis of spatial architecture in primary liver cancer. *Sci Adv* 7(51):eabg3750
27. Liu Y, Xun Z, Ma K, Liang S et al (2023) Identification of a tumour immune barrier in the HCC microenvironment that. *J Hepatol* 78(4):770–782
28. Ally A, Balasundaram M et al (2017) Comprehensive and integrative genomic characterization of hepatocellular carcinoma. *Cell* 169(7):1327–1341
29. Fernandez-Banet J, Lee NP, Chan KT, Gao H et al (2014) Decoding complex patterns of genomic rearrangement in hepatocellular carcinoma. *Genomics* 103(2–3):189–203
30. Murata K, Jadhav U, Madha S, van Es J et al (2020) Ascl2-dependent cell dedifferentiation drives regeneration of ablated intestinal. *Cell Stem Cell* 26(3):377–390
31. Stelzer G, Rosen N, Plaschkes I, Zimmerman S et al (2016) The geneCards suite: from gene data mining to disease genome sequence analyses. *Curr Protoc Bioinformatics* 54(1):1–1
32. Kayagaki N, Kornfeld OS et al (2021) NINJ1 mediates plasma membrane rupture during lytic cell death. *Nature* 591(7848):131–136
33. Degen M, Orcid Id, Santos JC, Orcid Id et al (2023) Structural basis of NINJ1-mediated plasma membrane rupture in cell death. *Nature* 17(10):023–05991
34. Zhou C, Lu X, Wang Y, Qian X et al (2022) Histopathological components correlated with MRI features and prognosis in. *Eur Radiol* 32(10):6702–6711
35. Zhang X, Ji L, Li MO (2023) Control of tumor-associated macrophage responses by nutrient acquisition and metabolism. *Immunity* 56(1):14–31
36. Liu Z, Gao Z, Li B, Li J et al (2022) Lipid-associated macrophages in the tumor-adipose microenvironment facilitate. *Oncimmunology* 11(1):2085432
37. Cheng K, Orcid Id, Cai N, Zhu J et al (2022) Tumor-associated macrophages in liver cancer: From mechanisms to therapy. *Cancer Commun* 42(11):1112–1140
38. Zhang YL, Li Q, Yang XM, Fang F et al (2018) SPON2 promotes M1-like macrophage recruitment and inhibits hepatocellular. *Cancer Res* 78(9):2305–2317
39. Zong Z, Zou J, Mao R et al (2019) M1 macrophages induce PD-L1 expression in hepatocellular carcinoma cells through IL-1 β signaling. *Front Immunol* 10:1643

Publisher's Note Springer Nature remains neutral with regard to jurisdictional claims in published maps and institutional affiliations.

Springer Nature or its licensor (e.g. a society or other partner) holds exclusive rights to this article under a publishing agreement with the author(s) or other rightsholder(s); author self-archiving of the accepted manuscript version of this article is solely governed by the terms of such publishing agreement and applicable law.

Authors and Affiliations

Chun Wang¹ · Cuimin Chen¹ · Wenting Hu¹ · Lili Tao¹ · Jiakang Chen¹

✉ Jiakang Chen
2228778160@qq.com

¹ Department of Pathology, Peking University Shenzhen Hospital, Shenzhen, Guangdong Province, China